Revista Internacional de Métodos Numéricos para Cálculo y Diseño en Ingeniería

Tech Science Press

https://doi.org/10.32604/rimni.2026.081596

ARTICLE

A Physics-Informed Neural Network Framework for Non-Newtonian Stagnation Point Flow with Cattaneo-Christov Heat Flux Effects

Mohd Vaseem[1], **Ziya Uddin**[1,2] **and Himanshu Upreti**[1,2,*]

[1]SoET, BML Munjal University, Gurugram, Haryana, India

[2]Center for Advanced Data and Computational Science, BML Munjal University, Gurugram, Haryana, India

*Corresponding Author: Himanshu Upreti. Email: hupretidream@gmail.com

Received: 05 March 2026; Accepted: 21 April 2026; Published: 06 November 2026

ABSTRACT: Non-Newtonian fluids, characterized by shear-rate-dependent viscosity, exhibit complex flow behaviors. This study examines the stagnation point flow and heat transfer characteristics of a tangent hyperbolic fluid, a non-Newtonian fluid model, over a flat plate. The plate surface is maintained at constant temperature and stretches with a linear velocity. The energy equation is modelled, incorporating the time-lag factor via the Cattaneo-Christov (CC) heat flux model, and is further, assisted with the non-uniform heat source/sink effect. The governing equations are transformed into ordinary differential equations (ODEs) using similarity transformations and solved using the Physics-Informed Neural Network (PINN), in which a deep neural network approximates the velocity and temperature field embedding the governing equations and boundary conditions into a composite loss function, trained without labeled data. The accuracy of the model is validated by comparing the computed local Nusselt number values with benchmark results from the literature, demonstrating excellent agreement. The findings of the study show that increasing the Weissenberg number reduces flow velocity and raises temperature, while higher values of the velocity ratio parameter enhance velocity and lower temperature due to stronger convective effects. An increase in the material power-law index leads to diminished velocity and elevated temperature, indicating shear-dependent behavior. Quantitatively, the magnitude of skin friction coefficient decreases by approximately 24.6% with increasing material parameter, while the local Nusselt number decreases by about 5.0%, indicating a reduction in the heat transfer rate. These results provide valuable insights into the control of heat transfer and flow characteristics in solar thermal systems, particularly in enhancing thermal efficiency of solar collectors and related energy conversion devices.

KEYWORDS: Tangent hyperbolic fluid; Cattaneo-Christov heat flux; stagnation point; flat plate; physics-informed neural network; wavelet activation function; solar thermal systems

1 Introduction

The study of non-Newtonian fluids has gained substantial attention recently due to its various applications in engineering and industries such as polymer processing, biofluids, and chemical manufacturing. Among the diverse range of non-Newtonian fluid models, the tangent hyperbolic fluid (THF) model has proved highly effective in representing shear-thinning behavior while maintaining mathematical tractability. Furthermore, when such fluids interact with the flat stretching surfaces, the resulting flow and thermal phenomena demand sophisticated modelling, especially under the influence of modern heat flux theories like the Cattaneo-Christov (CC) model. The stagnation point flow regime adds another layer of complexity and industrial relevance to such configurations. The following review presents significant literature classified according to these themes, highlighting both foundational and recent contributions.

Copyright © 2027 The Authors. Published by Tech Science Press. This work is licensed under a Creative Commons Attribution 4.0 International License, which permits unrestricted use, distribution, and reproduction in any medium, provided the original work is properly cited.

Tangent hyperbolic fluids (THFs) form a notable category of shear-thinning non-Newtonian materials whose behavior is captured through a constitutive model based on the hyperbolic tangent function. Such fluids arise frequently in processes involving polymers, biological fluids, food products like ketchup, and a variety of slurry-based materials. Akbar et al. [1] examined the boundary layer (BL) flow behavior of THFs under magnetohydrodynamic (MHD) effects over a stretching surface. Their numerical results revealed the pronounced effects of magnetic fields and nonlinearity inherent in THF on velocity profiles. Hayat et al. [2] conducted a study on the stagnation flow of a tangent hyperbolic nanofluid, incorporating nonlinear thermal radiation, highlighting the influence of double-diffusive convection mechanisms. Khan et al. [3] incorporated Wu's slip conditions, electrical MHD, and activation energy into a tangent hyperbolic nanofluid model, advancing electro-conductive applications. These studies highlighted the importance of non-Newtonian fluids in complex thermal systems. For example, Chu et al. [4] analyzed thermophoretic effects in Maxwell fluid flow, while Li et al. [5] examined Hall and viscous dissipation effects in Jeffrey nanofluid transport. Asogwa et al. [6] studied the electro-magnetohydrodynamic THF flow across a Riga surface incorporating the effects of Dufour diffusion and activation energy, while Hamad [7] examined MHD THF flow across a stretching surface with activation energy. Ahmadi Azar [8] analyzed dusty THF flow under thermal radiation and magnetic influences, emphasizing high Prandtl number conditions. These works emphasized the need for advanced modelling of nonlinear fluid and heat transfer behavior.

The analysis of boundary layer (BL) flow over a stretching flat plate is fundamental in understanding drag reduction, heat transfer, and material stretching in industrial processes. Aziz [9] presented one of the foundational works on laminar thermal BLs under convective conditions; Ishak [10] extended this to the permeable surfaces with convective heat transfer. Khan and Pop [11] introduced nanofluids into flat plate models, marking an advancement in thermal fluid modelling, and Makinde and Aziz [12] further investigated the nanofluid convection over stretching surfaces. Waqas et al. [13] investigated magneto-thixotropic nanofluid flow over a variable thickness surface, highlighting the significant influence of surface geometry on flow and heat transfer characteristics. Recently, Reddy et al. [14] provided a modern numerical investigation into tangent hyperbolic fluids over a stretching sheet, incorporating slip conditions to reflect real surface-fluid interactions.

Traditional Fourier's law suggests infinite thermal propagation speed, a physical inconsistency corrected by the CC heat flux model. This model modifies the classical theory by introducing a relaxation time and employing the material derivative, as formulated by Christov [15], ensuring frame indifference. Azhar et al. [16] validated this model in MHD THF flow over a porous surface, confirming its improved physical representation, and Naveen Kumar et al. [17] studied the influence of the CC heat flux model on nanofluid flow over a non-flat stretching boundary, integrating Stefan blowing effects, thereby highlighting the model's flexibility in complex thermal-fluid environments. Recent studies have also emphasized the significance of non-Fourier heat flux models in advanced thermal systems. For instance, Oreyeni et al. [18] investigated the CC heat flux model in bioconvective thixotropic fluid flow, highlighting its role in accurately capturing thermal transport behavior in energy storage applications.

Stagnation point flow occurs when fluid impinges directly on a surface, a situation frequently encountered in aerodynamic and industrial cooling systems. Hayat et al. [19] coupled this flow regime with the CC heat flux model and homogeneous-heterogeneous reactions, offering insights into chemical thermal systems. Mehmood et al. [20] addressed viscoelastic stagnation flow under CC flux, showing how relaxation effects and fluid elasticity influence the thermal profiles. In recent studies, Madhu et al. [21] analyzed the influence of nonlinear radiation and activation energy in hybrid nanofluid flow, while Ali Shah [22] examined micropolar bioconvection nanofluid flow over an inclined Riga plate. These studies highlighted the growing interest in complex stagnation-point flow configurations with advanced heat transfer mechanisms.

The recent study combines these complex phenomena into unified models to reflect real-world scenarios. Boujelbene et al. [23] analyzed CC heat flux in THF with thermal radiation over a stretching surface, emphasizing applications in renewable energy systems, and Salahuddin et al. [24] examined Darcy-Forchheimer flow of THF with radiation, viscous dissipation, and activation energy, capturing advanced industrial conditions. Kallem et al. [25] carried out an incorporation of irregular heat generation and Darcy-Forchheimer effects for a detailed numerical investigation of stagnation point flow involving a tangent hyperbolic nanofluid over a stretching surface, making it one of the most integrative and recent contributions in the domain.

Recent advancements in intelligent computational modelling have highlighted the power of Physics-Informed Neural Networks (PINNs) for solving complex fluid flow and heat transfer problems. Raissi et al. [26] pioneered the PINN framework as a unified deep-learning approach capable of solving the forward and inverse nonlinear differential equations problems without the need for mesh-based discretization. Building on this foundation, several researchers have extended PINNs and unsupervised neural-network strategies to nonlinear differential systems. For instance, Uddin et al. [27] developed a wavelet-based PINN architecture for efficiently solving nonlinear differential equations, while Sai et al. [28] applied unsupervised neural networks to model Maxwell fluid flow with nonlinear convection and temperature-dependent properties over curved geometries. Further innovations include the exploration of swirling Maxwell hybrid-nanofluid convection with nonlinear radiation using machine learning-based solvers by Sai et al. [29], and AI-driven thermal analysis of nano-encapsulated phase-change material fluids over wedge geometry by Upreti et al. [30]. More recently, PINN-based modelling of micropolar phase-change fluids over paraboloidal surfaces for solar-thermal applications was reported by Vaseem et al. [31]. For instance, Israr et al. [32] employed PINN-based methods for heat regulation of nanofluids, demonstrating their capability in accurately solving complex heat transfer problems in industrial applications. Collectively, these studies demonstrated the growing reliability and versatility of PINNs for tackling nonlinear, non-Newtonian, and thermally complex flows, However, despite these advancements, a clear gap still exists in the literature regarding the simultaneous investigation of THF behavior under CC heat flux within a stagnation-point flow configuration, particularly in the presence of non-uniform heat source/sink effects using a PINN framework.

Furthermore, most existing studies rely on conventional numerical solvers such as shooting or bvp4c methods, which often require strong initial guesses assumptions and may face convergence difficulties for highly nonlinear coupled systems. In contrast, the PINN framework offers a mesh-free alternative that directly incorporates the governing physics into the learning process, making it more flexible and robust for such complex problems.

The present study introduces the following key contributions:

- Integrates tangent hyperbolic fluid behavior with the CC heat flux model to account for thermal relaxation effects and enhance the physical realism of heat transfer.
- Analyses two-dimensional stagnation-point flow over a stretching flat plate under the influence of non-uniform heat source/sink.
- Applies a PINN framework to solve the highly nonlinear coupled governing equations, demonstrating its effectiveness as a mesh-free and robust alternative to traditional numerical methods.

2 Mathematical Formulation

The mathematical formulation of THF, a class of non-Newtonian fluids, is defined by a constitutive equation involving the hyperbolic tangent function to capture its shear-thinning behavior. The stress tensor is given by [1]:

$$\overline{\tau} = [\mu_\infty + (\mu_0 + \mu_\infty)\, tanh\,(\Gamma\dot{\gamma})^{\lambda}]A_a$$

where μ_0 and μ_∞ denote viscosities at zero and infinite shear rates, λ is the material (power law) index, Γ is the time-dependent material parameter, $\dot{\gamma}$ represents the shear rate, and A_a is the first Rivlin-Ericksen tensor.

For many practical non-Newtonian fluids, the infinite shear rate viscosity μ_∞ is significantly smaller than μ_0, and can therefore be neglected. Furthermore, for small values of $\Gamma\dot{\gamma} \ll 1$, the hyperbolic tangent function can be approximated using a first-order Taylor expansion as:

$$\tanh\,(\Gamma\dot{\gamma}) \approx \Gamma\dot{\gamma}$$

Using these assumptions, the constitutive relation simplifies to:

$$\overline{\tau} = \mu_0[1 + \lambda\,(\Gamma\dot{\gamma} - 1)]A_a$$

This approximation significantly reduces the mathematical complexity while retaining the essential shear-thinning characteristics of the fluid.

Consider the flow to be steady, laminar, and incompressible over a flat stretching surface aligned along the x-axis, with the fluid occupying the region $y \geq 0$. The plate stretches with a velocity $u_w(x)$, while the free-stream velocity is given by $u_e(x)$. Heat transfer within the fluid is characterized by a spatially varying heat source/sink and is governed by the Cattaneo-Christov (CC) model, which accounts for thermal relaxation effects beyond classical Fourier's law (Christov [15]). The physical configuration is illustrated in Fig. 1.

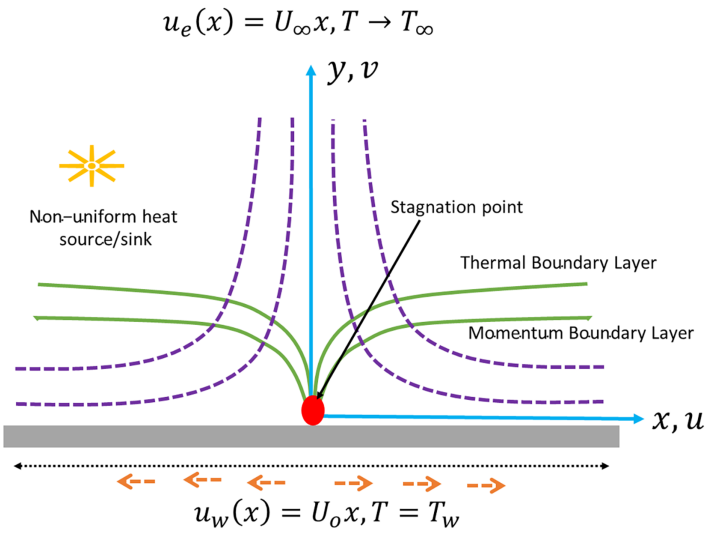


Figure 1: Geometry of the problem.

Based on boundary layer approximations, the governing equations for momentum and energy are formulated accordingly [23].

$$\frac{\partial u}{\partial x} + \frac{\partial v}{\partial y} = 0 \tag{1}$$

$$u\frac{\partial u}{\partial x} + v\frac{\partial u}{\partial y} = u_e(x)\frac{d}{dx}u_e(x) + \frac{\mu}{\rho}\left[(1-\lambda) + \lambda\Gamma\sqrt{2}\left(\frac{\partial u}{\partial y}\right)\right]\frac{\partial^2 u}{\partial y^2} \tag{2}$$

$$\rho C_P\left[u\frac{\partial T}{\partial x}+v\frac{\partial T}{\partial y}+\tau_o\left(u^2\frac{\partial^2 T}{\partial x^2}+v^2\frac{\partial^2 T}{\partial y^2}+\left(u\frac{\partial u}{\partial x}+v\frac{\partial u}{\partial y}\right)\frac{\partial T}{\partial x}+\left(u\frac{\partial v}{\partial x}+v\frac{\partial v}{\partial y}\right)\frac{\partial T}{\partial y}+2uv\frac{\partial^2 T}{\partial x\partial y}\right)\right]$$
$$=\kappa\frac{\partial^2 T}{\partial y^2}+\frac{\kappa u_w\left(T_w-T_\infty\right)}{x\vartheta}\left(A_1 f'+A_2\frac{T-T_\infty}{T_w-T_\infty}\right) \tag{3}$$

subject to the boundary conditions:

$$\left.\begin{array}{l} v=0, u=u_w(x)=U_o x, T=T_w \text{ at } y=0 \\ u\to u_e(x)=U_\infty x, T\to T_\infty \text{ as } y\to\infty \end{array}\right\} \tag{4}$$

Here, the variables u, v represent the velocity components along the x and y-directions directions, respectively. The variable $\rho(\mathrm{Kgm}^{-3})$ represents the density of the fluid, while the variable $\mu(\mathrm{Kgm}^{-1}\mathrm{s}^{-1})$ is the dynamic viscosity, $C_P(\mathrm{Jkg}^{-1}\mathrm{K}^{-1})$ denotes the specific heat capacity, $T_o(\mathrm{s})$ is the thermal relaxation time, $\kappa(\mathrm{Wm}^{-1}\mathrm{K}^{-1})$ is the fluid's thermal conductivity. Furthermore, the parameters A_1 and A_2 characterize the space-dependent heat source/sink effects, where A_1 represents the non-uniform heat generation associated with the flow field, and A_2 corresponds to temperature—dependent heat absorption or generation within the fluid.

To reduce Eqs. (1)–(3) along with (4) into a system of ODEs, the following similarity transformations are introduced [11,12]:

$$\left.\begin{array}{l} \eta=y\sqrt{\dfrac{U_o}{\vartheta}}, \psi(x,y)=\sqrt{U_o\vartheta}xf(\eta), \theta=\dfrac{T-T_\infty}{T_w-T_\infty}, \\ u=\dfrac{\partial\psi}{\partial y}=U_o x f'(\eta), v=-\dfrac{\partial\psi}{\partial x}=-\sqrt{U_o\vartheta}f(\eta) \end{array}\right\} \tag{5}$$

These transformations are applicable to steady, two-dimensional boundary layer flow over a linearly stretching surface with velocity $u_w(x)=U_o x$, for which the governing equations admit similarity solutions.

Substituting Eq. (5) into Eqs. (1)–(3), Eq. (1) is identically satisfied, while Eqs. (2) and (3), together with boundary conditions (4), are transformed to the following dimensionless ODEs (see Appendix A for details).

$$(1-\lambda)f'''-f'^2+ff''+\lambda We f''f'''+A^2=0 \tag{6}$$

$$\frac{1}{Pr}\theta''-\frac{1}{Pr}\left(A_1 f'+A_2\theta\right)+f\theta'-\tau\left[f^2\theta''+ff'\theta'\right]=0 \tag{7}$$

with

$$\left.\begin{array}{l} f(\eta)=0, f'(\eta)=1, \theta(\eta)=1, at\eta=0 \\ f'(\infty)\to A, \theta(\infty)\to 0 as\eta\to\infty \end{array}\right\} \tag{8}$$

Here $\left(We=\Gamma u_w\sqrt{\frac{2U_o}{\vartheta}}\right)$ represents the Weissenberg number, $\left(Pr=\frac{\vartheta(\rho C_p)}{\kappa}\right)$ represents the Prandtl number, $\left(A=\frac{U_\infty}{U_o}\right)$ represents the velocity ratio variable, $(\tau=U_o\tau_o)$ denotes the thermal relaxation parameter and λ is the material power law index.

The skin friction coefficient (SFC) C_f and the local Nusselt number (LNN) Nu_x are [11]

$$C_f = \frac{\tau_w}{\rho\,(u_w(x))^2}, Nu_x = \frac{xq_w}{\kappa(T_w - T_\infty)} \tag{9}$$

where τ_w is the wall shear stress and q_w is the heat flux at the surface, which are given by

$$\tau_w = \mu\left((1-\lambda)\frac{\partial u}{\partial y} + \frac{\lambda\Gamma}{\sqrt{2}}\left(\frac{\partial u}{\partial y}\right)^2\right)\Bigg|_{y=0}, q_w = -\kappa\frac{\partial T}{\partial y}\Bigg|_{y=0} \tag{10}$$

Substituting Eq. (10) into Eq. (9) and employing (5), we obtain:

$$\left.\begin{aligned} C_f Re^{\frac{1}{2}} &= \left((1-\lambda)f''(0) + \tfrac{\lambda}{2}Wef''(0)^2\right) and \\ Nu_x Re^{-\frac{1}{2}} &= -\theta'(0) \end{aligned}\right\} \tag{11}$$

where $Re = \dfrac{xu_w}{\vartheta}$ is local Reynolds number.

3 Methodology

To model the governing differential equations (DEs) describing the stagnation point flow and heat transfer of a THF, the PINN framework is employed. PINNs embed the governing physical laws into the loss function of a neural network, enabling simultaneous learning of the solution and enforcement of physical constraints. This mesh-free methodology is particularly effective for highly nonlinear and coupled thermo-fluid systems. The present formulation follows the pioneering work of Raissi et al. [26], and its subsequent applications in complex transport problems [28–31].

The architecture of the PINN model is illustrated in Fig. 2, where the neural networks approximate the solution fields while the governing equations and boundary conditions are enforced through residual minimization.

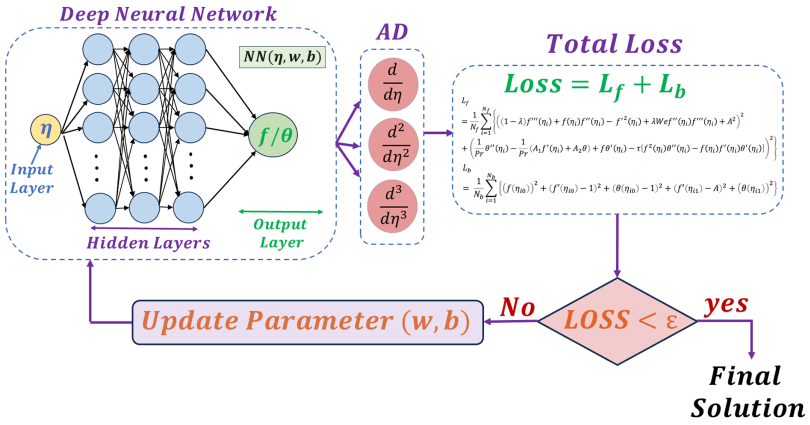


Figure 2: Schematic diagram of the PINN architecture showing input variable η_i, hidden layers, outputs $f_i(\eta)$ and $\theta_i(\eta)$, and residual connections used for computing L_f and L_b.

3.1 Neural Network Representation

The solution variables are approximated using two separate neural networks, each trained using identical optimization settings (optimizer, learning rate, and activation function), while the number of hidden layers and neurons is tailored separately for each network:

$$f(\eta) \approx \hat{f}(\eta; W_f, b_f), \theta(\eta) \approx \hat{\theta}(\eta; W_\theta, b_\theta)$$

where W and b denote the weights and biases of the respective networks, and the subscripts f and θ correspond to the velocity and temperature fields, respectively. The velocity network consists of 4 hidden layers with 30 neurons in each layer, whereas the temperature network comprises 6 hidden layers with 60 neurons per layer, providing enhanced representational capacity for capturing the thermal field. The trainable parameters are initialized using the Xavier (Glorot) initialization scheme, which ensures stable variance propagation across layers.

3.2 Activation Function

A Gaussian wavelet activation function is employed in all hidden layers to improve approximation capability for boundary layer-type solutions. The adopted activation function is expressed as:

$$\phi(x) = xe^{\left(-\frac{x^2}{2}\right)}$$

This wavelet-based activation provides localized feature extraction and superior representation of steep gradients compared to conventional smooth activations, making it particularly suitable for non-Newtonian boundary layer flows, as reported in [27].

3.3 Loss Function Construction

The total loss function is formulated as:

$$L = L_f + L_b$$

where the physics loss is given by:

$$L_f = \frac{1}{N_f}\sum_{i=1}^{N_f}\left\{\left((1-\lambda) f'''(\eta_i) + f(\eta_i) f''(\eta_i) - f'^2(\eta_i) + \lambda We f''(\eta_i) f'''(\eta_i) + A^2\right)^2 + \left(\frac{1}{Pr}\theta''(\eta_i) - \frac{1}{Pr}(A_1 f'(\eta_i) + A_2\theta) + f\theta'(\eta_i) - \tau\left[f^2(\eta_i)\theta''(\eta_i) - f(\eta_i) f'(\eta_i)\theta'(\eta_i)\right]\right)^2\right\}$$

and the boundary loss is defined as:

$$L_b = \frac{1}{N_b}\sum_{i=1}^{N_b}\left\{\left(f(\eta_{i0})\right)^2 + \left(f'(\eta_{i0}) - 1\right)^2 + \left(\theta(\eta_{i0}) - 1\right)^2 + \left(f'(\eta_{i1}) - A\right)^2 + \left(\theta(\eta_{i1})\right)^2\right\}$$

Here, N_f = 10,000 and N_b = 500 denote the number of collocation and boundary points, respectively. The boundary points η_j correspond to the physical constraints imposed at $\eta = 0$ and $\eta \to \infty$. All the derivatives are computed using automatic differentiation applied independently to each neural network, ensuring high numerical accuracy without discretization error.

3.4 Collocation Strategy and Domain Analysis

The collocation points are randomly sampled within the computational domain $\eta \in [0, 3]$. To ensure domain adequacy, a domain-independence analysis is conducted by extending the computational domain beyond $\eta = 3$. The results indicate negligible variation in velocity, temperature, SFC, and LNN, confirming that $\eta_{max} = 3$ is sufficient to capture the asymptotic decay of the solution.

3.5 Training Procedure

The optimization problem is solved using the Adam optimizer with a learning rate of 10^{-4}, minimizing the total loss function ($L \leq 10^{-5}$). A fixed random seed is used to ensure reproducibility of the results. The model is implemented in the TensorFlow framework, and all computations are performed on a standard computational setup.

3.6 Model Validation

To validate the accuracy of the proposed PINN framework, the wall heat transfer rate $-\theta'(0)$ is computed and compared with previously published results for varying Prandtl number Pr, while keeping other parameters fixed as:

$$A_1 = 0 = A_2, \tau = 0, We = 0, A = 0, \lambda = 0$$

As shown in Table 1, the present results exhibit excellent agreement with [33,34], confirming the validity and robustness of the proposed approach. Furthermore, a direct comparison between the present PINN predictions and numerical solutions obtained using the MATLAB bvp4c solver is presented in Fig. 3a,b for both velocity and temperature profiles, demonstrating excellent consistency between the two approaches.

Table 1: Comparison of numerical values of $-\theta'(0)$.

Pr	Devi and Devi [33]	Waini et al. [34]	Present Results
2	0.91135	0.911353	0.9117882
6.13	1.75968	1.759682	1.7501237
7	1.89540	1.895400	1.8861945
20	3.35390	3.353902	3.3340702

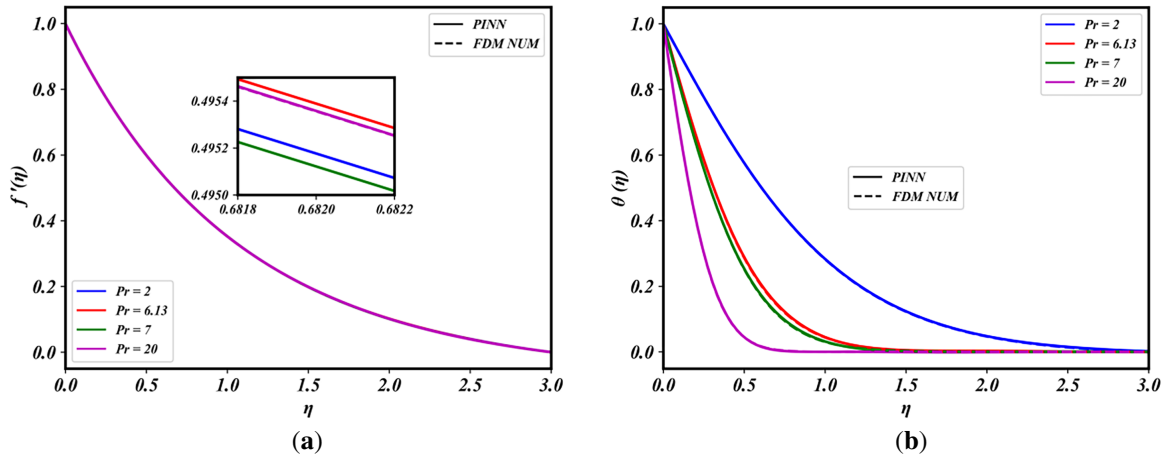


Figure 3: (**a**) Comparison of velocity profile for varying Pr. (**b**) Comparison of temperature profile for varying Pr.

4 Results and Discussion

This section presents an in-depth analysis of the influence of varying parameters on flow behavior derived from the proposed PINN framework. The computations are carried out with fixed values of $Pr = 7$, $A_1 = 0.2 = A_2$, and $\tau = 0.1$, while systematically varying parameters We, A, λ. The selected parameter ranges are based on values reported in the literature and are consistent with realistic operating conditions in solar thermal systems. The Cattaneo-Christov heat flux model is employed to incorporate thermal relaxation effects, which overcome the limitation of infinite heat propagation speed associated with classical Fourier's law. The effects of these parameters are illustrated through velocity and temperature distributions (see Figs. 4–6). Furthermore, their impact on the skin friction coefficient (SFC), which provides insight into shear stress behavior at the surface, and the local Nusselt number (LNN)-characterizes surface heat flux is computed and presented in Table 2 for the corresponding parametric variations.

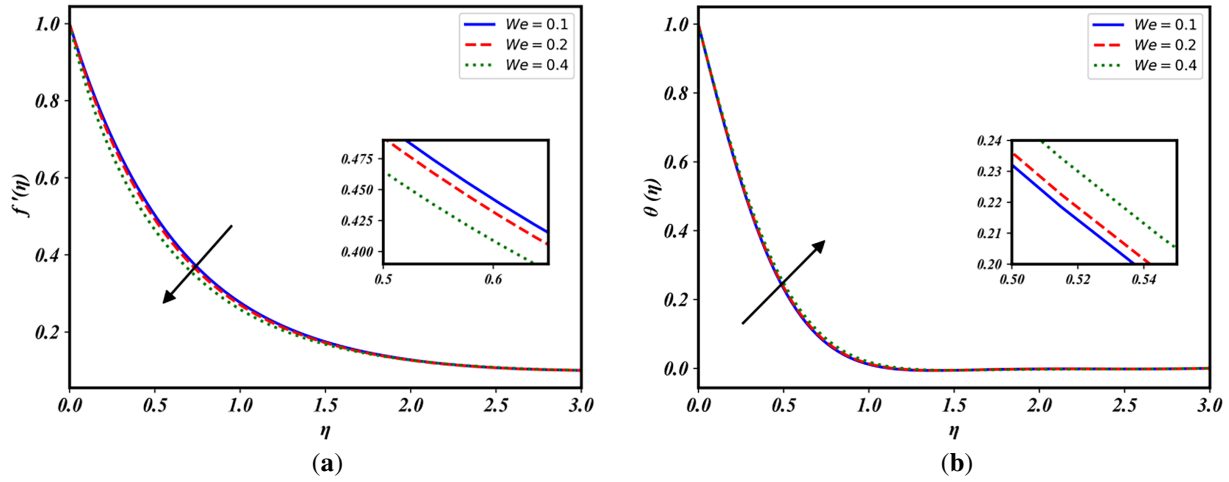


Figure 4: (**a**) Velocity profile for We. (**b**) Temperature profile for We.

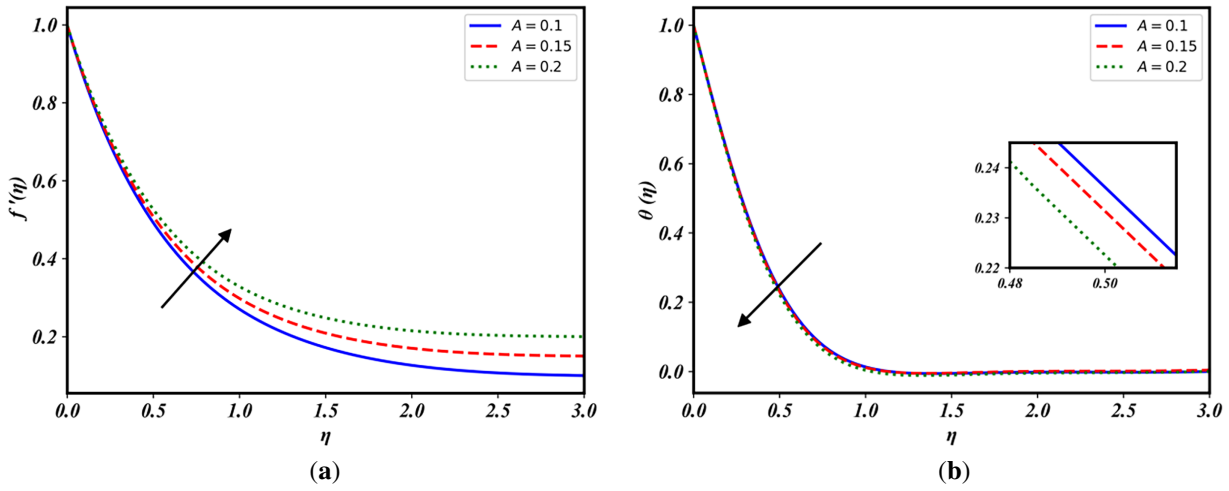


Figure 5: (**a**) Velocity profile for A. (**b**) Temperature profile for A.

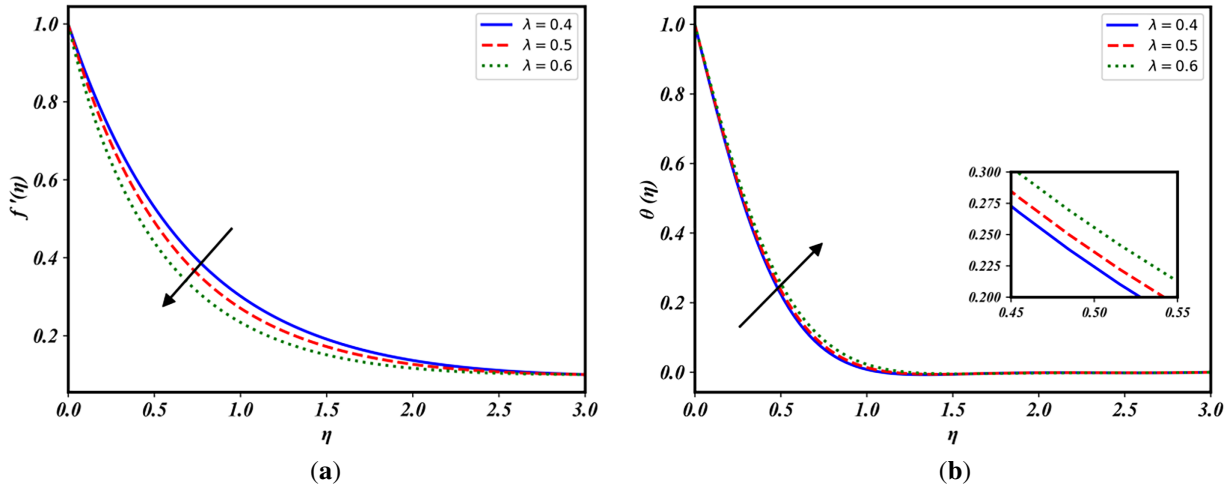


Figure 6: (**a**) Velocity profile for λ. (**b**) Temperature profile for λ.

Table 2: Computed the values of $|C_f Re^{1/2}|$ and the $Nu_x Re^{-1/2}$ when $Pr = 7$ and $A_1 = 0.2 = A_2$, $\tau = 0.1$.

We	λ	A	$\lvert C_f Re^{1/2}\rvert$	$Nu_x Re^{-1/2}$
0.1	0.5	0.1	0.66746575	1.9808197
0.2			0.64710474	1.9674130
0.4			0.59068420	1.9262013
0.2	0.4		0.72711710	2.0055122
	0.5		0.64710474	1.9674130
	0.6		0.54786164	1.9054294
	0.5	0.1	0.64710474	1.9674130
		0.15	0.63215530	1.9826853
		0.2	0.61460350	2.0055520

Fig. 4a,b shows the impact of the We on the fluid velocity and temperature profiles. An increase in We leads to a decline in velocity, accompanied by a thinning of the BL. This behaviour is attributed to the enhanced elastic nature of the fluid, which resists deformation and slows the motion. Physically, the stored elastic energy within the fluid opposes the shear-induced deformation, thereby suppressing momentum diffusion across the BL. Conversely, the temperature profile exhibits an increase with rising We, particularly evident at lower values We, indicating that fluid elasticity exerts a more substantial influence on momentum transfer than on thermal diffusion in this range. This enhancement in temperature can be associated with reduced convective transport due to slower fluid motion, which allows more heat to accumulate within the BL region. Moreover, due to thermal relaxation, heat propagation occurs at a finite speed, which further enhances thermal accumulation within the BL compared to Fourier conduction. The combined influence of fluid elasticity and non-Fourier heat flux leads to a comparatively thicker thermal BL.

The influence of A on the profiles is depicted in Fig. 5a,b. An increase in A enhances the fluid velocity, as higher values of A suggest dominance of the free-stream velocity over the surface velocity, intensifying the flow near the stagnation region. This results in a stronger stretching of fluid layers, which promotes momentum transport and elevates the velocity within the BL. On the other hand, temperature decreases with

increasing A, a consequence of the reduced thermal BL thickness due to the accelerated surface flow, which enhances convective heat removal. Physically, the intensified convection limits heat accumulation near the surface, leading to a thinner thermal BL and lower temperature distribution. In addition, the presence of thermal relaxation moderates the rate of heat diffusion, while the dominance of stretching and stagnation flow enhances convective transport. This reflects a competing interaction between surface stretching and finite-speed heat propagation in shaping the thermal field.

In Fig. 6a,b, the behavior of the λ is examined. As λ increases, a noticeable drop in velocity and a concurrent rise in temperature are observed. This is indicative of shear-thickening fluid behavior, where increased resistance to flow reduces velocity but enhances energy dissipation as heat, thereby elevating temperature levels. Physically, the higher effective viscosity associated with larger λ suppresses fluid motion and thickens the momentum BL. Simultaneously, the increased internal friction generates additional thermal energy, contributing to the rise in temperature within the BL. Furthermore, the coupling of shear-dependent viscosity with thermal relaxation significantly alters heat transport characteristics, while the non-uniform heat source/sink contributes to either augmentation or suppression of temperature within the BL. This demonstrates a strong interaction between rheological and thermal mechanisms.

Fig. 7a,b illustrates the effect of spatially varying heat source parameters on the temperature distribution. In Fig. 7a, A_1 is varied while $A_2 = 0.2$ is kept fixed, whereas in Fig. 7b, A_2 is varied with $A_1 = 0.2$ held constant. It is observed that an increase in A_1 results in a noticeable reduction in temperature within the BL. Physically, a positive value of A_1 represents a space-dependent heat generation mechanism associated with the flow field. Larger values of A_1 correspond to the heat source being located farther away from the surface of the plate.

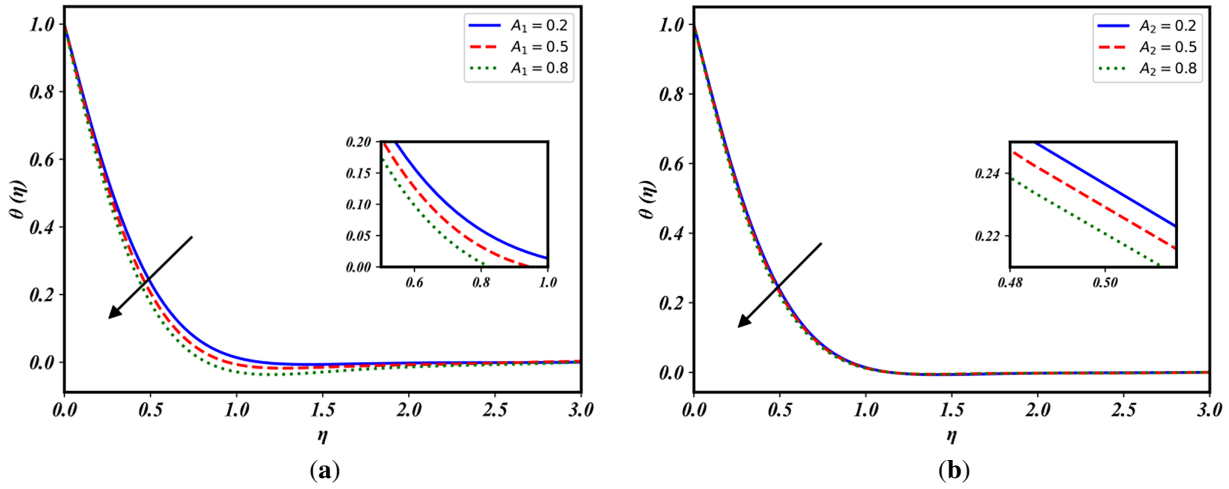


Figure 7: (**a**) Temperature profile for $A_1 > 0$ & $A_2 = 0.2$. (**b**) Temperature profile for $A_2 > 0$ & $A_1 = 0.2$.

From the velocity profiles, it is evident that the velocity $f'(\eta)$ decreases with increasing distance from the plate. Consequently, the combined effect of a higher A_1 and the decaying $f'(\eta)$ reduces the effectiveness of heat generation within the BL. As a result, the temperature decreases with increasing η for larger values of A_1, see Fig. 7a. Similarly, increasing the values of A_2, which represents temperature-dependent heat generation, also leads to a decrease in temperature, as shown in Fig. 7b.

In contrast, Fig. 8a,b represents the heat sink case. In Fig. 8a, A_1 is varied while $A_2 = -0.2$ is fixed, whereas in Fig. 8b, A_2 is varied with $A_1 = -0.2$ held constant. In this scenario, increasing the magnitude of the negative parameters A_1 or A_2 leads to an increase in temperature. Although a more negative value of A_1 represents a stronger heat sink, it is also associated with the spatial positioning of the heat sink away from the

plate. Since $f'(\eta)$ decreases with distance from the surface, the combined effect of spatial variation and the decaying $f'(\eta)$ reduces the effective influence of the heat sink within the BL. Consequently, increasing the negative magnitude of A_1 weakens the overall cooling effect, resulting in a rise in temperature, see Fig. 8a. A similar trend is observed for the temperature-dependent heat sink parameter A_2, as depicted in Fig. 8b, where increasing its negative magnitude also leads to an increase in temperature.

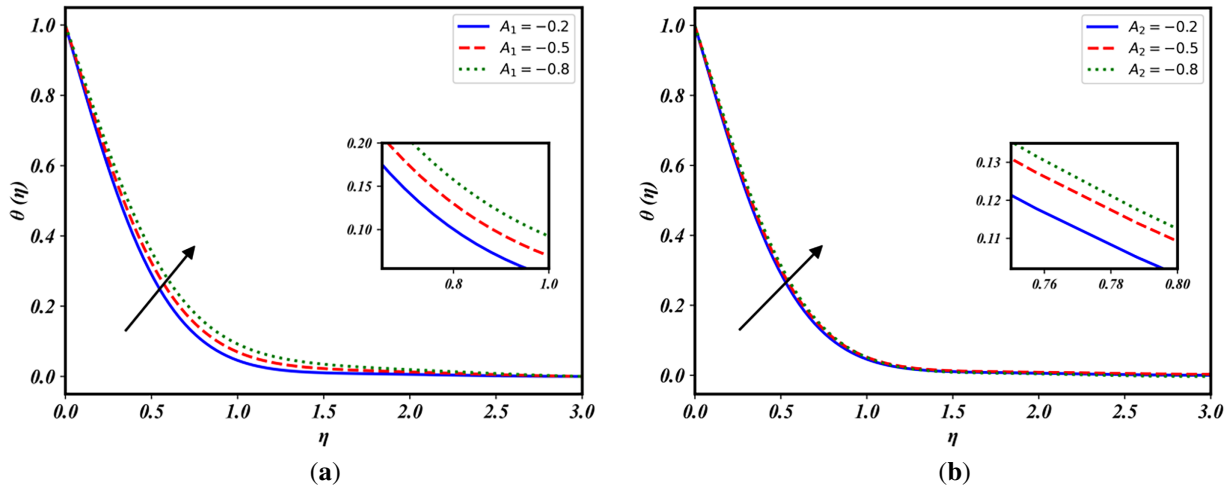


Figure 8: (**a**) Temperature profile for $A_1 < 0$ & $A_2 = -0.2$ fixed. (**b**) Temperature profile for $A_2 < 0$ & $A_1 = -0.2$ fixed.

From Table 2, it is observed that the magnitude of the skin friction coefficient (SFC) consistently decreases with increasing We, λ, and A. Quantitatively, SFC declines by approximately 11.5% as We increases $(0.1-0.4)$, 24.6% with $\lambda(0.4-0.6)$, and about 5.0% with $A(0.1-0.2)$. This reduction reflects the combined influence of fluid elasticity and enhanced viscous resistance, which suppresses the velocity gradients at the wall and weakens the shear stress.

Similarly, the local Nusselt number (LNN) also decreases by nearly 2.8% with increasing We and 5.0% with λ, whereas it increases by about 2.0% with higher A. Physically, higher We and λ reduce convective transport due to slower fluid motion and increased internal resistance, leading to weaker heat transfer. In contrast, increasing A accelerates the flow near the surface, strengthens convection, and consequently enhances the heat transfer rate.

5 Conclusions

This study presents a PINN-based approach to model the stagnation point flow and heat transfer of THF over a flat plate, incorporating CC heat flux and the effect of heat source/sink. The model successfully captures the nonlinear behavior of non-Newtonian fluids under thermal relaxation and is validated by benchmarking results against existing literature, confirming its accuracy and physical reliability. Moreover, the proposed framework demonstrates strong capability in handling complex coupled thermo-fluid problems without relying on traditional mesh-based numerical schemes.

Key findings from the analysis include:

- Increasing We reduces velocity and slightly increases temperature due to stronger fluid elasticity.
- Increasing the A enhances fluid flow and reduces temperature via convective heat removal.
- A higher λ leads to lower velocity and higher temperature, reflecting shear-thickening behaviour.

- SFC shows limited variation with changes in parameters, while the LNN decreases with We and λ but increases with A.

From an application perspective, these findings are particularly relevant to solar thermal systems, where control of heat transfer and fluid behavior is crucial for improving thermal efficiency. The ability to regulate temperature distribution through fluid elasticity and flow parameters can be beneficial in optimizing solar collectors and thermal energy storage devices.

Furthermore, the inclusion of thermal relaxation effects provides a more realistic description of heat transport in high-temperature solar applications, where classical Fourier assumptions may become inadequate.

In future work, the present model can be extended to more complex geometries, variable heat source/sink conditions, and hybrid nanofluids to further enhance its applicability in advanced solar thermal technologies. Additionally, sensitivity analysis, experimental validation and real-system integration may provide deeper insights into practical implementation.

Acknowledgement: None

Funding Statement: The authors received no specific funding for this study.

Author Contributions: Mohd Vaseem: Conceptualization, Methodology, Visualization, Writing—original draft. Ziya Uddin: Conceptualization, Methodology, Supervision, Writing—reviewing and editing. Himanshu Upreti: Conceptualization, Supervision, Writing—reviewing and editing. All authors reviewed and approved the final version of the manuscript.

Availability of Data and Materials: Not applicable.

Ethics Approval: Not applicable.

Conflicts of Interest: The authors declare no conflicts of interest.

Appendix A

For a non-dimensional form, following similarity transformations are used

$$\eta = y\sqrt{\frac{U_o}{\vartheta}}, \psi(x,y) = \sqrt{U_o \vartheta} x f(\eta), \theta = \frac{T - T_\infty}{T_w - T_\infty} \tag{A1}$$

where, $\psi(x,y)$ is the stream function, and $u = \frac{\partial \psi}{\partial y}$ and $v = -\frac{\partial \psi}{\partial x}$.

$$u = \frac{\partial}{\partial y}\sqrt{U_o \vartheta} x f\left(y\sqrt{\frac{U_o}{\vartheta}}\right), \text{and } v = -\frac{\partial}{\partial x}\sqrt{U_o \vartheta} x f\left(y\sqrt{\frac{U_o}{\vartheta}}\right)$$

By evaluating the partial derivatives and rearranging, the velocity components take the forms

$$u = U_o x f'^{(\eta)}, v = -\sqrt{U_o \vartheta} f(\eta) \tag{A2}$$

By differentiating the velocity components u and v, as well as the temperature T, with respect to x and y are

$$\frac{\partial u}{\partial x} = U_o f'(\eta) \tag{A3}$$

$$\frac{\partial u}{\partial y} = xU_o\left(\sqrt{\frac{U_o}{\vartheta}}\right)f''(\eta) \tag{A4}$$

$$\frac{\partial^2 u}{\partial y^2} = x\frac{{U_o}^2}{\vartheta}f'''(\eta) \tag{A5}$$

$$\frac{\partial v}{\partial x} = 0 \tag{A6}$$

$$\frac{\partial v}{\partial y} = -U_o f'(\eta) \tag{A7}$$

$$\frac{\partial T}{\partial x} = 0 \tag{A8}$$

$$\frac{\partial T}{\partial y} = (T_w - T_\infty)\left(\sqrt{\frac{U_o}{\vartheta}}\right)\theta'(\eta) \tag{A9}$$

$$\frac{\partial^2 T}{\partial x^2} = 0 \tag{A10}$$

$$\frac{\partial^2 T}{\partial y^2} = (T_w - T_\infty)\frac{U_o}{\vartheta}\theta''(\eta) \tag{A11}$$

$$\frac{\partial^2 T}{\partial x \partial y} = \frac{\partial}{\partial x}\left(\frac{\partial T}{\partial y}\right) = \frac{\partial}{\partial x}\left((T_w - T_\infty)\left(\sqrt{\frac{U_o}{\vartheta}}\right)\theta'(\eta)\right) = 0 \tag{A12}$$

Continuity equation:

$$\frac{\partial u}{\partial x} + \frac{\partial v}{\partial y} = 0 \tag{A13}$$

$=\gg \frac{\partial}{\partial x}\{xU_o f'(\eta)\} + \frac{\partial}{\partial y}\left\{-\sqrt{U_o\vartheta}f(\eta)\right\} = 0$ is identically satisfied.

Momentum equation:

$$u\frac{\partial u}{\partial x} + v\frac{\partial u}{\partial y} = u_e(x)\frac{d}{dx}u_e(x) + \frac{\mu}{\rho}\left[(1-\lambda) + \lambda\Gamma\sqrt{2}\left(\frac{\partial u}{\partial y}\right)\right]\frac{\partial^2 u}{\partial y^2} \tag{A14}$$

$$=\gg \{xU_o f'(\eta)\}\frac{\partial}{\partial x}\{xU_o f'(\eta)\} + \left\{-\sqrt{U_o\vartheta}f(\eta)\right\}\frac{\partial}{\partial y}\{xU_o f'(\eta)\} = \{xU_\infty\}\frac{d}{dx}\{xU_\infty\}$$
$$+ \frac{\mu}{\rho}\left[(1-\lambda) + \lambda\Gamma\sqrt{2}\left(\frac{\partial}{\partial y}\{xU_o f'(\eta)\}\right)\right]\frac{\partial^2}{\partial y^2}\{xU_o f'(\eta)\}$$
$$=\gg \{xU_o f'(\eta)\}U_o f'(\eta) + \left\{-\sqrt{U_o\vartheta}f(\eta)\right\}\left\{xU_o\sqrt{\frac{U_o}{\vartheta}}f''(\eta)\right\} = \{xU_\infty\}U_\infty$$
$$+ \frac{\mu}{\rho}\left[(1-\lambda) + \lambda\Gamma\sqrt{2}\left(xU_o\sqrt{\frac{U_o}{\vartheta}}f''(\eta)\right)\right]\frac{x{U_o}^2}{\vartheta}f'''(\eta)$$

simplifying the equation, yields the reduced ordinary differential equation is

$$(1-\lambda)\,f''' - f'^2 + ff'' + \lambda We f'' f''' + A^2 = 0 \tag{A15}$$

where $We = \Gamma u_w \sqrt{\frac{2U_o}{\vartheta}}$ is the Weissenberg number, $A = \frac{U_\infty}{U_o}$ is the velocity ratio parameter.

Energy Equation:

$$\rho C_P \left[u\frac{\partial T}{\partial x} + v\frac{\partial T}{\partial y} + \tau_o \left(u^2\frac{\partial^2 T}{\partial x^2} + v^2\frac{\partial^2 T}{\partial y^2} + \left(u\frac{\partial u}{\partial x} + v\frac{\partial u}{\partial y} \right)\frac{\partial T}{\partial x} + \left(u\frac{\partial v}{\partial x} + v\frac{\partial v}{\partial y} \right)\frac{\partial T}{\partial y} + 2uv\frac{\partial^2 T}{\partial x \partial y} \right) \right] = \kappa\frac{\partial^2 T}{\partial y^2} + \frac{\kappa u_w (T_w - T_\infty)}{x\vartheta} \left(A_1\frac{\partial f}{\partial \eta} + A_2\frac{T - T_\infty}{T_w - T_\infty} \right) \tag{A16}$$

Using the definition of u and v from Eq. (A2), we obtain

$$\begin{aligned} \Rightarrow\gg \rho C_P \Bigg[& \{U_o x f'(\eta)\}\frac{\partial T}{\partial x} + \left\{-\sqrt{U_o \vartheta} f(\eta)\right\}\frac{\partial T}{\partial y} + \tau_o \Bigg(\{U_o x f'(\eta)\}^2\frac{\partial^2 T}{\partial x^2} + \left\{-\sqrt{U_o\vartheta} f(\eta)\right\}^2\frac{\partial^2 T}{\partial y^2} \\ & + \left(\{U_o x f'(\eta)\}\frac{\partial u}{\partial x} + \left\{-\sqrt{U_o\vartheta} f(\eta)\right\}\frac{\partial u}{\partial y} \right)\frac{\partial T}{\partial x} + \left(\{U_o x f'(\eta)\}\frac{\partial v}{\partial x} + \left\{-\sqrt{U_o\vartheta} f(\eta)\right\}\frac{\partial v}{\partial y} \right)\frac{\partial T}{\partial y} \\ & + 2\{U_o x f'(\eta)\}\left\{-\sqrt{U_o\vartheta} f(\eta)\right\}\frac{\partial^2 T}{\partial x \partial y} \Bigg) \Bigg] = \kappa\frac{\partial^2 T}{\partial y^2} + \frac{\kappa u_w (T_w - T_\infty)}{x\vartheta} \left(A_1\frac{\partial f}{\partial \eta} + A_2\frac{T - T_\infty}{T_w - T_\infty} \right) \end{aligned} \tag{A17}$$

The corresponding partial derivatives are expressed in Eqs. (A3)–(A12). Substituting these expressions into equation

$$\begin{aligned} \Rightarrow\gg C_P \Bigg[& \{U_o x f'(\eta)\} \times 0 + \left\{-\sqrt{U_o\vartheta} f(\eta)\right\} \times \left\{ (T_w - T_\infty)\left(\sqrt{\frac{U_o}{\vartheta}}\right)\theta'(\eta) \right\} \\ & + \tau_o \Bigg(\{U_o x f'(\eta)\}^2 \times 0 + \left\{-\sqrt{U_o\vartheta} f(\eta)\right\}^2 \times \left\{ (T_w - T_\infty)\frac{U_o}{\vartheta}\theta''(\eta) \right\} \\ & + \Bigg(\{U_o x f'(\eta)\} \times \{U_o f'(\eta)\} + \left\{-\sqrt{U_o\vartheta} f(\eta)\right\} \times \left\{ x U_o \left(\sqrt{\frac{U_o}{\vartheta}}\right) f''(\eta) \right\} \Bigg) \times 0 \\ & + \Big(\{U_o x f'(\eta)\} \times 0 + \left\{-\sqrt{U_o\vartheta} f(\eta)\right\} \times \{-U_o f'(\eta)\} \Big) \times \left\{ (T_w - T_\infty)\left(\sqrt{\frac{U_o}{\vartheta}}\right)\theta'(\eta) \right\} \\ & + 2 \times \{U_o x f'(\eta)\} \times \left\{-\sqrt{U_o\vartheta} f(\eta)\right\} \times 0 \Big) \Bigg] = \kappa \left\{ (T_w - T_\infty)\frac{U_o}{\vartheta}\theta''(\eta) \right\} \\ & + \frac{\kappa u_w (T_w - T_\infty)}{x\vartheta} \left(A_1 f'(\eta) + A_2\theta(\eta) \right) \end{aligned} \tag{A18}$$

and simplifying the equation, yield the reduced non-dimensional energy equation of the form

$$\frac{1}{Pr}\theta'' - \frac{1}{Pr}\left(A_1 f' + A_2\theta \right) + f\theta' - \tau\left[f^2\theta'' + ff'\theta' \right] = 0 \tag{A19}$$

where $Pr = \frac{\vartheta(\rho C_p)}{\kappa}$ denotes the Prandtl number, and $\tau = U_o\tau_o$ represents the thermal relaxation parameter based on the CC heat flux model.

References

1. Akbar NS, Nadeem S, Haq RU, Khan ZH. Numerical solutions of Magnetohydrodynamic boundary layer flow of tangent hyperbolic fluid towards a stretching sheet. Indian J Phys. 2013;87(11):1121–4. doi:10.1007/s12648-013-0339-8.
2. Hayat T, Qayyum S, Alsaedi A, Ali Shehzad S. Nonlinear thermal radiation aspects in stagnation point flow of tangent hyperbolic nanofluid with double diffusive convection. J Mol Liq. 2016;223:969–78. doi:10.1016/j.molliq.2016.08.102.
3. Khan SU, Waqas H, Shehzad SA, Imran M. Theoretical analysis of tangent hyperbolic nanoparticles with combined electrical MHD, activation energy and Wu's slip features: a mathematical model. Phys Scr. 2019;94(12):125211. doi:10.1088/1402-4896/ab399f.
4. Chu YM, Sadiq Hashmi M, Khan N, Ullah Khan S, Ijaz Khan M, Kadry S, et al. Thermophoretic particles deposition features in thermally developed flow of Maxwell fluid between two infinite stretched disks. J Mater Res Technol. 2020;9(6):12889–98. doi:10.1016/j.jmrt.2020.09.011.
5. Li P, Abbasi A, El-Zahar ER, Farooq W, Hussain Z, Khan SU, et al. Hall effects and viscous dissipation applications in peristaltic transport of Jeffrey nanofluid due to wave frame. Colloid Interface Sci Commun. 2022;47(1):100593. doi:10.1016/j.colcom.2022.100593.
6. Asogwa KK, Goud BS, Ali Shah N, Yook SJ. Rheology of electromagnetohydrodynamic tangent hyperbolic nanofluid over a stretching riga surface featuring dufour effect and activation energy. Sci Rep. 2022;12(1):14602. doi:10.1038/s41598-022-18998-9.
7. Hamad NH. Numerical investigation of MHD tangent hyperbolic nanofluid flow across a vertical stretching surface subject to activation energy. J Therm Anal Calorim. 2023;148(22):12687–97. doi:10.1007/s10973-023-12548-9.
8. Ahmadi Azar A. Thermal radiation and magnetic field effects on dusty hyperbolic tangent fluid flow over a stretching sheet with high Prandtl number. Int Commun Heat Mass Transf. 2025;165(1):109040. doi:10.1016/j.icheatmasstransfer.2025.109040.
9. Aziz A. A similarity solution for laminar thermal boundary layer over a flat plate with a convective surface boundary condition. Commun Nonlinear Sci Numer Simul. 2009;14(4):1064–8. doi:10.1016/j.cnsns.2008.05.003.
10. Ishak A. Similarity solutions for flow and heat transfer over a permeable surface with convective boundary condition. Appl Math Comput. 2010;217(2):837–42. doi:10.1016/j.amc.2010.06.026.
11. Khan WA, Pop I. Boundary-layer flow of a nanofluid past a stretching sheet. Int J Heat Mass Transf. 2010;53(11–12):2477–83. doi:10.1016/j.ijheatmasstransfer.2010.01.032.
12. Makinde OD, Aziz A. Boundary layer flow of a nanofluid past a stretching sheet with a convective boundary condition. Int J Therm Sci. 2011;50(7):1326–32. doi:10.1016/j.ijthermalsci.2011.02.019.
13. Waqas M, Dogonchi AS, Shehzad SA, Khan MI, Hayat T, Alsaedi A. Nonlinear convection and joule heating impacts in magneto-thixotropic nanofluid stratified flow by convectively heated variable thicked surface. J Mol Liq. 2020;300:111945. doi:10.1016/j.molliq.2019.111945.
14. Reddy BN, Dodda R, Reddy BS. A numerical investigation on boundary layer flow of MHD tangent hyperbolic fluid flow over a stretching sheet with slip boundary conditions. J Adv Res Fluid Mech Therm Sci. 2024;120(1):122–39. doi:10.37934/arfmts.120.1.122139.
15. Christov CI. On frame indifferent formulation of the Maxwell–Cattaneo model of finite-speed heat conduction. Mech Res Commun. 2009;36(4):481–6. doi:10.1016/j.mechrescom.2008.11.003.
16. Azhar E, Iqbal Z, Maraj EN, Ahmad B. Influence of Cattaneo-Christov heat flux model on mhd hyperbolic tangent fluid over a moving porous surface. Front Heat Mass Transf. 2017;8:1–7. doi:10.5098/hmt.8.25.
17. Naveen Kumar R, Suresh Goud J, Srilatha P, Manjunatha PT, Rani SP, Kumar R, et al. Cattaneo–Christov heat flux model for nanofluid flow over a curved stretching sheet: an application of Stefan blowing. Heat Transf. 2022;51(6):4977–91. doi:10.1002/htj.22532.
18. Oreyeni T, Shamshuddin MD, Obalalu AM, Saeed A, Ali Shah N. Exploring the impact of stratification on the dynamics of bioconvective thixotropic fluid conveying tiny particles and Cattaneo-Christov model: thermal storage system application. Propuls Power Res. 2024;13(3):416–32. doi:10.1016/j.jppr.2024.08.002.

19. Hayat T, Khan MI, Farooq M, Yasmeen T, Alsaedi A. Stagnation point flow with Cattaneo-Christov heat flux and homogeneous-heterogeneous reactions. J Mol Liq. 2016;220:49–55. doi:10.1016/j.molliq.2016.04.032.
20. Mehmood Y, Sagheer M, Hussain S, Bilal M. MHD stagnation point flow and heat transfer in viscoelastic fluid with Cattaneo–Christov heat flux model. Neural Comput Appl. 2018;30(10):2979–86. doi:10.1007/s00521-017-2902-2.
21. Madhu J, Madhukesh JK, Sarris I, Prasannakumara BC, Ramesh GK, Ali Shah N, et al. Influence of quadratic thermal radiation and activation energy impacts over oblique stagnation point hybrid nanofluid flow across a cylinder. Case Stud Therm Eng. 2024;60(9):104624. doi:10.1016/j.csite.2024.104624.
22. Ali Shah N. Stagnation point on the micropolar bioconvection nanofluid flow over inclined Riga plate: keller box analysis. Phys Fluids. 2025;37(1):012013. doi:10.1063/5.0250554.
23. Boujelbene M, Majeed A, Ijaz N, Bakouri M, Ching DLC, Khan I, et al. Cattaneo-Christov heat flux theory in tangent hyperbolic hybrid nanofluids with thermal radiation for renewable energy applications. J Radiat Res Appl Sci. 2024;17(4):101139. doi:10.1016/j.jrras.2024.101139.
24. Salahuddin T, Maryum Kalsoom S, Awais M, Khan M, Altanji M. Impact of Darcy-Forchheimer for the flow analysis of radiated tangent hyperbolic fluid with viscous dissipation and activation energy. Int J Hydrogen Energy. 2024;72(2):949–57. doi:10.1016/j.ijhydene.2024.05.425.
25. Kallem SR, Sheri SR, Perli AP, Helal MM, Ismail AI. Numerical investigation of tangent hyperbolic nanofluid with stagnation point flow of irregular heat and Darcy-Forchheimer effects on stretching sheet. Results Eng. 2025;27(1):105821. doi:10.1016/j.rineng.2025.105821.
26. Raissi M, Perdikaris P, Karniadakis GE. Physics-informed neural networks: a deep learning framework for solving forward and inverse problems involving nonlinear partial differential equations. J Comput Phys. 2019;378:686–707. doi:10.1016/j.jcp.2018.10.045.
27. Uddin Z, Sai G, Asthana R, Ibrahim W. Wavelets based physics informed neural networks to solve non-linear differential equations. Sci Rep. 2023;13(1):2882. doi:10.1038/s41598-023-29806-3.
28. Sai G, Uddin Z, Asthana R. Unsupervised neural networks for Maxwell fluid flow and heat transfer over a curved surface with nonlinear convection and temperature-dependent properties. Int J Numer Methods Fluids. 2024;96(9):1576–91. doi:10.1002/fld.5298.
29. Sai G, Uddin Z, Asthana R. Exploring swirling flow dynamics: unsupervised machine learning in Maxwell hybrid nanofluid convection over an exponentially stretching cylinder with non-linear radiation effects. Commun Nonlinear Sci Numer Simul. 2025;140(9):108378. doi:10.1016/j.cnsns.2024.108378.
30. Upreti H, Uddin Z, Vaseem M. Unsupervised AI-driven numerical study of flow and heat transfer analysis of nano-encapsulated phase change material nanofluid over wedge. AI Therm Fluids. 2025;2–3:100009. doi:10.1016/j.aitf.2025.100009.
31. Vaseem M, Uddin Z, Upreti H. Physics informed neural network-based study of phase-change micropolar fluid flow over Paraboloidal surface: solar thermal applications. Int Commun Heat Mass Transf. 2025;169:109645. doi:10.1016/j.icheatmasstransfer.2025.109645.
32. Israr M, Ayub A, Alkhalaf A, Ali B, Ali Shah N. AI-assisted PDFP-based PINNs for heat regulation of nanofluid in industrial cooling enclosures around circular barriers. Int Commun Heat Mass Transf. 2026;173(8):110717. doi:10.1016/j.icheatmasstransfer.2026.110717.
33. Devi SU, Devi SA. Heat transfer enhancement of Cu-Al_2O_3/water hybrid nanofluid flow over a stretching sheet. J Niger Math Soc. 2017;36:419–33.
34. Waini I, Ishak A, Pop I. Unsteady flow and heat transfer past a stretching/shrinking sheet in a hybrid nanofluid. Int J Heat Mass Transf. 2019;136(6):288–97. doi:10.1016/j.ijheatmasstransfer.2019.02.101.